

Suppression of the stellar enhancement factor and the reaction $^{85}\text{Rb}(p,n)^{85}\text{Sr}$

T. Rauscher,^{1,*} G. G. Kiss,² Gy. Gyürky,² A. Simon,² Zs. Fülöp,² and E. Somorjai²

¹*Department of Physics, University of Basel, CH-4056 Basel, Switzerland*

²*Institute of Nuclear Research (ATOMKI), H-4001 Debrecen, POB.51., Hungary*

(Dated: October 29, 2018)

It is shown that a Coulomb suppression of the stellar enhancement factor occurs in many endothermic reactions at and far from stability. Contrary to common assumptions, reaction measurements for astrophysics with minimal impact of stellar enhancement should be preferably performed for those reactions instead of their reverses, despite of their negative Q value. As a demonstration, the cross section of the astrophysically relevant $^{85}\text{Rb}(p,n)^{85}\text{Sr}$ reaction has been measured by activation between $2.16 \leq E_{\text{c.m.}} \leq 3.96$ MeV and the astrophysical reaction rates at p process temperatures for (p,n) as well as (n,p) are directly inferred from the data. Additionally, our results confirm a previously derived modification of a global optical proton potential. The presented arguments are also relevant for other α - and proton-induced reactions in the p , rp , and νp processes.

PACS numbers: 26.50.+x Nuclear physics aspects of novae, supernovae, and other explosive environments, 24.60.Dr Statistical compound-nucleus reactions, 27.50.+e $59 \leq A \leq 89$

I. INTRODUCTION

Astrophysical reaction rates are central to tracing changes in the abundances of nuclei by nuclear reactions. They provide the temperature- and density-dependent coefficients entering reaction networks, the large sets of coupled differential equations required to study nucleosynthesis and energy generation in astrophysical environments. The reaction rates are computed from reaction cross sections which, in turn, may be predicted in theoretical models or extracted from experiments. In addition to the difficulties arising in the determination of the cross sections, the conversion to reaction rates is further complicated by modifications of the rates in a hot plasma and the fact that the rates of forward and reverse rate for the same reaction have to be consistent to ensure numerical stability and proper equilibrium abundances at high temperature. Both issues can be addressed at once by accounting for the thermal population of target states which leads to *stellar* rates obeying a reciprocity relation between forward and reverse rate. Using this reciprocity, knowledge of the rate in only one direction is needed because the other reaction direction can be directly computed from that rate, thus ensuring consistency.

For numerical reasons, further elaborated in Sec. II B, it is usually preferable to start from the rate of a reaction with positive reaction Q value when computing the rate for its inverse reaction. Even more importantly, experimentalists want to determine rates as close as possible to the actual stellar rates, i.e. rates with minimal thermal population effects of the target. Again, it can be argued that this is the case for exothermic reactions. This led to the commonly applied rule that measurements of exothermic reactions are more important than those of endothermic ones. In this paper we show that there is a

considerable number of reactions for which a suppression effect brings the stellar rate of an endothermic reaction closer to the laboratory value than its exothermic counterpart.

As an example of how to exploit this suppression effect and to obtain stellar rates from a measurement of an endothermic reaction, we experimentally studied the reaction $^{85}\text{Rb}(p,n)^{85}\text{Sr}$, having $Q = -1.847$ MeV. The importance of the reaction is manifold. In the last several years a number of proton capture cross section measurements with relevance for γ process studies have been carried out (see, e.g., [1] and references therein). The γ process was shown to synthesize p nuclides (proton-rich isotopes not accessible to the s and r processes) by a series of photodisintegrations of stable nuclides in hot layers of massive stars [2, 3, 4, 5]. Recently, systematic γ process simulations found not only that photodisintegration reactions are important but also that (p,n) reactions, and in particular $^{85}\text{Rb}(p,n)^{85}\text{Sr}$, strongly influence the final p abundances [6]. Additionally, this reaction is well suited to test the optical potential used for calculating the interaction between protons and target nuclei.

We commence by outlining the theoretical background regarding stellar rates and the suppression effect in Secs. II A and II B. The results of a large-scale study of the effect in the full extension of the nuclear chart are discussed in Sec. II C. Focusing on the reaction $^{85}\text{Rb}(p,n)^{85}\text{Sr}$, their relevance is discussed in Sec. III A, the experimental details are provided in Secs. III B–III D, and the astrophysically relevant rates are derived in Sec. III G. Additionally, Sec. III F discusses implications of our new experimental results for the proton optical potential. Finally, a summary is given in Sec. IV.

A brief account of our findings was already given in [7]. The present follow-up paper expands the discussion and also provides additional results in all parts of this investigation.

*Electronic address: Thomas.Rauscher@unibas.ch

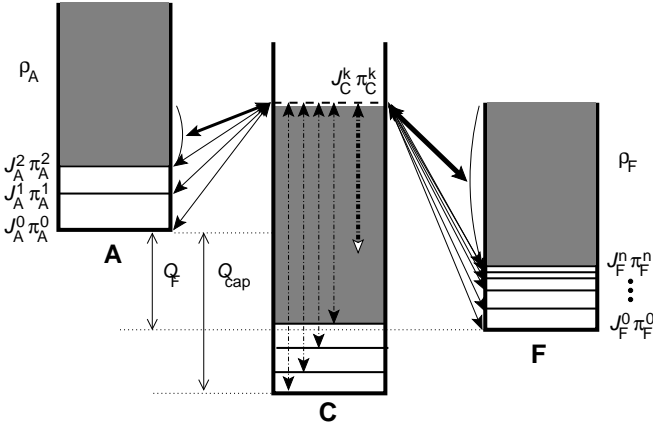


FIG. 1: Schematic view of the transitions (full arrows denote particle transitions, dashed arrows are γ transitions) in a compound reaction involving the nuclei A and F, and proceeding via a compound state (horizontal dashed line) with spin J_C^k and parity π_C^k in the compound nucleus C. The reaction Q values for the capture reaction (Q_{cap}) and the reaction $A \rightarrow F$ (Q_F) are given by the mass differences of the involved nuclei. The effective cross section σ^{eff} (Eqs. 4 and 6) for a reaction type is a sum over all energetically possible transitions to bound states (capture: in nuclei A and C; otherwise: in nuclei A and F) from the compound level as shown here (see text for details). In each nucleus, a number of low-lying states with given spin J and parity π is explicitly specified. Above the last state, transitions can be computed by integrating over nuclear level densities (shaded areas). In stellar cross sections σ^* all transitions are additionally weighted by a Boltzmann distribution factor depending on the stellar temperature, spin, and the excitation energy of the involved state (see Eq. 3).

II. SUPPRESSION OF THE STELLAR ENHANCEMENT

A. Stellar reaction rates

The stellar enhancement factor (SEF) f is defined as the ratio of the stellar rate r^* relative to the ground state rate $r^{\text{g.s.}}$ [8]

$$f = \frac{r^*}{r^{\text{g.s.}}} = \frac{r^*}{r^{\text{lab}}} \quad . \quad (1)$$

The rate r^{lab} derived from cross sections σ^{lab} measured in the laboratory is the same as $r^{\text{g.s.}}$ because so far all experiments use target nuclei in their ground states. The SEF is a measure of the influence of the thermally excited target states in the hot plasma.

Astrophysical reaction rates are usually defined as giving the number of a specific reaction occurring per time. Here, we constrain ourselves to two-body reactions of nuclei and nucleons. The concept of the stellar rates suppression introduced below is easily extended to other reaction types. Reaction cross sections are folded with the energy distribution of the interacting nuclei to obtain the reaction rate. The energy distributions of nuclei

and nucleons in an astrophysical plasma follow Maxwell-Boltzmann distributions in most applications, thus yielding [8]

$$\begin{aligned} r_i &= \frac{n_1 n_2}{1 + \delta_{12}} \frac{F}{(kT)^{3/2}} \int_0^\infty \sigma_i E e^{-\frac{E}{kT}} dE \\ &= \frac{n_1 n_2}{1 + \delta_{12}} \mathcal{R}_i \end{aligned} \quad (2)$$

for reactions proceeding from target state i with reaction cross section σ_i , where n_1 , n_2 are the number densities of the interacting nuclei, T is the plasma temperature, k denotes the Boltzmann constant, and F is a renormalization factor $F = \sqrt{8/(\pi\mu)}$ with $\mu = A_1 A_2 / (A_1 + A_2)$ being the reduced mass number A .

When nuclei are in thermal equilibrium with their environment, their excited states are populated according to a Boltzmann factor [8]

$$P_i = \frac{(2J_i + 1) e^{-\frac{E_i}{kT}}}{\sum_n (2J_n + 1) e^{-\frac{E_n}{kT}}} \quad , \quad (3)$$

with P_i , J_i , E_i denoting the relative population, spin, and excitation energy of state i , respectively. Each of the states is bombarded with Maxwell-Boltzmann distributed projectiles which would require to have a separate rate for each target state weighted by the population factor of the state i from which the reaction proceeds. It was shown in [9] (see also [10]) that by making use of the reciprocity theorem for nuclear reactions and detailed balance (assuming thermalization of both initial and final states of a reaction), for compound reactions the rate equation can be simplified to

$$\begin{aligned} \mathcal{R}^* &= \frac{F}{(kT)^{3/2}} \sum_i \left(\int_0^\infty P_i(T) \sigma_i(E^i) E^i e^{-\frac{E^i}{kT}} dE^i \right) \\ &= \frac{(2J^0 + 1) F}{(kT)^{3/2} G} \int_0^\infty \sigma^{\text{eff}}(E) E e^{-\frac{E}{kT}} dE \quad , \end{aligned} \quad (4)$$

$$r^* = \frac{n_1 n_2}{1 + \delta_{12}} \mathcal{R}^* \quad . \quad (5)$$

In order to avoid additional computations caused by the population coefficients and also to avoid having a temperature dependent stellar cross section, the effective cross section σ^{eff} was introduced above, which sums over all bound states in the initial *and* final system (denoted by i and j , respectively; the energetics of the transitions is shown in Fig. 1) [10]:

$$\sigma^{\text{eff}} = \sum_i \sum_j \sigma_{ij} \quad . \quad (6)$$

This is a theoretical construct (as any measurement would always proceed on a certain initial state and thus neglect the sum over target states) but it is useful in two respects. Firstly, it simplifies the computation of the rate and therefore is utilized in all *astrophysical* compound reaction codes. Secondly, it allows us to easily find a reciprocity relation between forward and inverse rate by remembering that $E\sigma^{\text{eff}}$ obeys reciprocity between forward

and inverse reaction due to detailed balance. It should be noted that only *stellar* reactivities \mathcal{R}^* (and thus stellar rates r^*) obey reciprocity (as long as detailed balance is applicable) whereas rates derived from ground state cross sections $\sigma^{\text{lab}} = \sum_j \sigma_{0j}$ do not, unless the SEF is equal to unity in the given direction.

For reactions $1 + 2 \rightarrow 3 + 4$ with target nucleus 1, projectile 2, final nucleus 3, and ejectile 4, the relation between backward and forward stellar reactivity is given by [8, 11]

$$\mathcal{R}_{34}^* = \frac{(2J_2^0 + 1)}{(2J_4^0 + 1)} \left(\frac{A_1 A_2}{A_3 A_4} \right)^{3/2} \frac{G_1}{G_3} e^{-\frac{Q_{12}}{kT}} \mathcal{R}_{12}^* \quad , \quad (7)$$

where Q_{12} is the reaction Q value, J^0 denote ground state spins, and G are nuclear partition functions summing over states i and integrating over a level density ρ above the last discrete state m included [10, 11]:

$$G(T) = \sum_{i=0}^m (2J_i + 1) e^{-\frac{E_i}{kT}} + \int_{E_m}^{E^{\text{max}}} \sum_{J,\pi} (2J + 1) e^{-\frac{E}{kT}} \rho(E, J, \pi) dE \quad . \quad (8)$$

This partition function also appears in Eq. 4 where it is sufficient to compute it once and separately from the rate integration.

Stellar capture reactions $1 + 2 \rightarrow 3 + \gamma$ are related to stellar photodisintegration by [10, 11]

$$\mathcal{R}_{3\gamma}^* = (2J_2^0 + 1) \left(\frac{A_1 A_2}{A_3} \right)^{3/2} \left(\frac{kT}{2\pi\hbar^2} \right)^{3/2} \frac{G_1}{G_3} e^{-\frac{Q_{12}}{kT}} \mathcal{R}_{12}^* \quad . \quad (9)$$

B. Reaction Q value and stellar enhancement factor

Figure 1 shows a sketch of the energetically allowed transitions included in the effective cross section defined by Eq. (6). It is obvious that there are more transitions possible to and from states of the nucleus being the final nucleus in a reaction with positive Q value. Therefore, assuming a similar level structure in all involved nuclei, it is expected that the SEF (see Eq. 1) of a given reaction will be smaller for the exothermic direction f_{forw} than for the endothermic one f_{rev} (here we define the forward reaction to be the one with positive Q value and the reverse reaction having negative Q value):

$$f_{\text{rev}} > f_{\text{forw}} \quad . \quad (10)$$

This is especially pronounced in photodisintegration reactions due to the many possible γ transitions [12, 13]. In consequence, aiming at performing a measurement as close as possible to the stellar value, an exothermic reaction should be chosen.

Another impact of the Q value is found by inspection of Eqs. (7) and (9) where the Q value appears in an exponential. For numerical consistency and to obtain proper equilibrium abundances when forward and reverse reaction are both fast and in equilibrium, reaction network codes avoid employing separate rates for the two directions but rather make use of these equations. Taking an endothermic reaction as starting point for application of the equations would lead to a large value of the exponential term, amplifying any numerical errors inherent in the original rate and in the Q value. This is mainly important when dealing with rate fits. In many astrophysical reaction network codes, the rates are implemented not as large tables but as fits with a smaller number of parameters per reaction. Any deficiency in the fit would be amplified when computing an exothermic rate from an endothermic one.

For the above reasons, it was commonly assumed that it is always preferable to determine the cross section and rate of an exothermic reaction and not those of an endothermic one. Here, we want to correct that notion by showing that there are cases for which

$$f_{\text{rev}} < f_{\text{forw}} \quad . \quad (11)$$

The basic idea is to realize that although there are more transitions energetically possible to the final states of exothermic reactions, some of them may be suppressed and thus not contributing. Of course, it is obvious that not all transitions are of equal strength. Quantum mechanical spin and parity selection rules and centrifugal barriers (or lack thereof) may prefer certain transitions over others. This will be important in reactions with small $|Q|$ and in nuclei with large level spacings. In both cases, only a small number of transitions will be possible and the spins can give larger weight to an even smaller subset. However, for reactions with sizeable Q values or involving nuclei with high level densities this suppression due to spins will not be sufficient because there will always be a number of states with matching spins.

Transitions to higher lying excited states of a nucleus proceed at lower relative energy. Except for s-wave neutrons, also transitions at lower relative energy will be weaker than those at larger relative energy. If the suppression of transitions with smaller relative energy is different in the entrance and exit channel of the reaction, this may also result in $f_{\text{rev}} < f_{\text{forw}}$. The strongest suppression for charged particles is due to the Coulomb barrier. Having different Coulomb barriers in the entrance and exit channel, e.g. in (n,p) or (p, α) reactions, can more strongly suppress the transitions to the nucleus with higher Coulomb barrier than to the one with lower Coulomb barrier. With respect to Fig. 1 and assuming, e.g., a reaction $A(n,\alpha)F$ this means that most transitions to states in nucleus F are suppressed and the contributing transitions may be fewer than those accessing states in nucleus A.

This Coulomb suppression of the SEF is a general principle almost independent of nuclear structure and will act

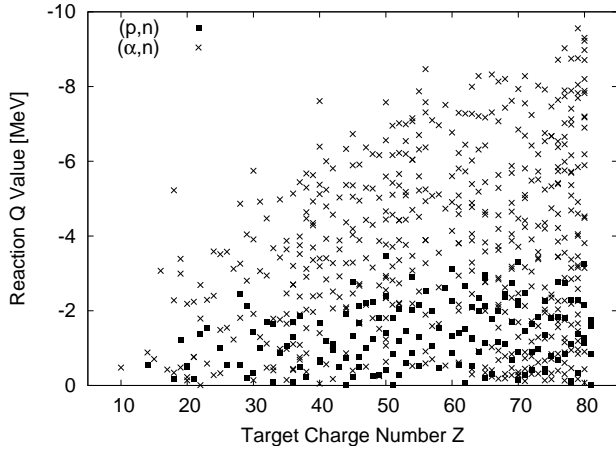


FIG. 2: Reaction Q values for (p,n) and (α ,n) reactions with $f_{\text{rev}} < f_{\text{forw}}$.

for a large range of nuclei. Whether the suppression is strong enough to yield $f_{\text{rev}} < f_{\text{forw}}$ depends on the size of the Q value relative to the Coulomb barrier, i.e. the effect can occur in a reaction provided that there are different Coulomb barriers in the entrance and exit channel and $|Q|$ is low compared to the Coulomb barrier. The strongest impact is to be expected when the forward reaction involves neutrons in the entrance channel which form a compound state by s-waves on excited target states and charged particles experiencing a high Coulomb barrier in the exit channel. As discussed in Sec. III G the reaction $^{85}\text{Rb}(p,n)^{85}\text{Sr}$ is an excellent example for such a case. A quantitative exploration of the suppression effect across the nuclear chart is given in the following section.

Not only theoretically interesting, this Coulomb suppression effect is also important for experiments because it allows to directly determine an astrophysically relevant rate by measuring in the direction of suppressed SEF. The above mentioned complication of fitting rates with negative Q values can be circumvented by directly applying detailed balance and numerically computing the rate for the forward reaction before performing a fit. This is possible when $f_{\text{rev}} \approx 1$. Subsequently, fits for both rates can be obtained in the standard way. As an example, an application of this procedure to the rate of $^{85}\text{Rb}(p,n)^{85}\text{Sr}$ is shown in Sec. III G.

C. Exploration of the SEF suppression across the nuclear chart

In this section, we quantitatively study the SEF suppression introduced and discussed in the previous section. Using NON-SMOKER results [11, 14] we compared f_{forw} and f_{rev} for reactions involving light projectiles (nucleons, α) and targets from Ne to Bi between the proton and neutron driplines. To avoid trivial cases, only reactions with $f_{\text{forw}}/f_{\text{rev}} \geq 1.1$ are considered. Furthermore, the SEF were computed for $T \leq 4.5$ GK to find cases

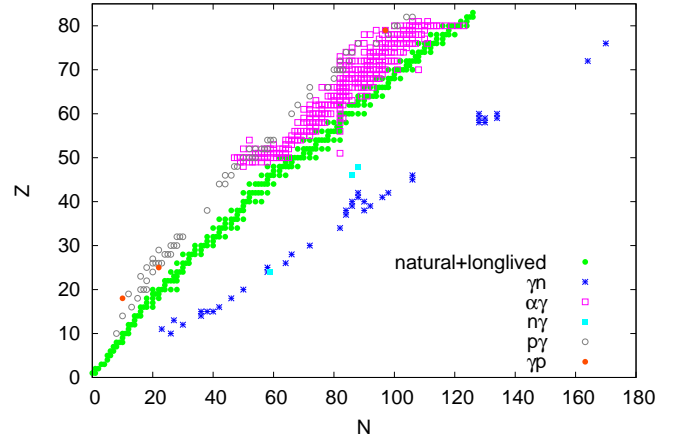


FIG. 3: (Color online) Targets for endothermic reactions with $f_{\text{rev}} < f_{\text{forw}}$ in the nuclear chart, where charge is denoted by Z and neutron number by N . The reaction type is given by the label. Only capture or photodisintegration reactions are shown. Also printed for orientation are stable and longlived nuclides.

important in most nucleosynthesis environments and to eliminate cases only occurring at high temperature. Because of our aim to provide guidance for experiments, we further only focus on examples with $f_{\text{rev}} \leq 1.5$. Even with these restrictions we find 1200 reactions exhibiting such a strong suppression effect that $f_{\text{rev}} < f_{\text{forw}}$.

To check the dependence on the Coulomb barrier, Fig. 2 shows the obtained range of Q values still yielding $f_{\text{rev}} < f_{\text{forw}}$ as a function of target charge Z for (p,n) and (α ,n) reactions with negative Q values. It can be clearly seen that larger maximal $|Q|$ is allowed with increasing charge Z . The different increase in permitted maximal $|Q|$ is different for the two reactions, reflecting the difference in the height of the acting Coulomb barriers. Below each maximally allowed $|Q|$ for each given charge, there is a range of other values. This scatter is mainly caused by the available Q values (as defined by the masses of the nuclei) and not by other effects such as spins and parities of the involved nuclei. Although the strengths of the involved transitions also depend on spin and parity of the initial and final state, Coulomb repulsion dominates the suppression when the interaction energy is small, as it is the case for astrophysically relevant energies.

Tables I–V list the reactions found to have $f_{\text{rev}} < f_{\text{forw}}$ according to the criteria discussed above. Stable or longlived target nuclei are marked specifically. Figures 3 and 4 locate the reactions in the nuclear chart.

To current knowledge, not all shown reactions are of astrophysical importance. Others may be too far from stability to be accessible to experiments. Figure 3 displays capture or photodisintegration reactions. Of particular importance among them are the (α , γ) reactions, also given in Table I. They are located in a mass region which is of interest in the p - or γ -process [2, 3]. Although the γ process synthesizes nuclei via photodis-

TABLE I: Targets for (α, γ) reactions with negative Q value but smaller SEF than their inverse reaction. Stable or longlived targets are in italics.

⁹⁸ Cd	¹⁰⁴ Te	¹³⁰ Ce	¹⁴³ Eu	¹⁵⁰ Er	¹⁵³ Lu	¹⁷³ W	¹⁷⁸ Pt
⁹⁸ In	¹⁰⁶ Te	¹³¹ Ce	¹⁴⁵ Eu	¹⁵¹ Er	¹⁵⁵ Lu	¹⁷⁴ W	¹⁷⁹ Pt
⁹⁹ In	¹⁰⁹ Te	¹³² Ce	¹⁴⁷ Eu	¹⁵² Er	¹⁵⁶ Lu	¹⁷⁶ W	¹⁸⁰ Pt
¹⁰¹ In	¹¹⁰ Te	¹³³ Ce	¹⁴⁹ Eu	¹⁵³ Er	¹⁶² Lu	¹⁷⁷ W	¹⁸¹ Pt
¹⁰² In	¹¹¹ Te	¹³⁴ Ce	¹⁴² Gd	¹⁵⁴ Er	¹⁶³ Lu	¹⁶¹ Re	¹⁸² Pt
¹⁰³ In	¹¹² Te	¹³⁵ Ce	¹⁴³ Gd	¹⁵⁵ Er	¹⁶⁶ Lu	¹⁶⁷ Re	¹⁸³ Pt
¹⁰⁵ In	¹¹⁴ Te	¹⁴⁰ Ce	¹⁴⁴ Gd	¹⁵⁶ Er	¹⁶⁷ Lu	¹⁷¹ Re	¹⁸⁴ Pt
¹⁰⁷ In	¹¹⁵ Te	¹²⁹ Pr	¹⁴⁵ Gd	¹⁵⁷ Er	¹⁵⁴ Hf	¹⁷² Re	¹⁸⁵ Pt
⁹⁷ Sn	¹¹⁶ Te	¹³¹ Pr	¹⁴⁶ Gd	¹⁵⁸ Er	¹⁵⁶ Hf	¹⁷⁵ Re	¹⁸⁶ Pt
⁹⁸ Sn	¹¹⁷ Te	¹³³ Pr	¹⁴⁷ Gd	¹⁵⁹ Er	¹⁵⁷ Hf	¹⁷⁹ Re	¹⁸⁷ Pt
⁹⁹ Sn	¹¹³ I	¹³⁵ Pr	¹⁴⁸ Gd	¹⁶⁰ Er	¹⁵⁸ Hf	¹⁶⁴ Os	¹⁷³ Au
¹⁰⁰ Sn	¹¹⁷ I	¹⁴¹ Pr	¹⁴⁹ Gd	¹⁶¹ Er	¹⁵⁹ Hf	¹⁶⁶ Os	¹⁷⁶ Au
¹⁰¹ Sn	¹¹⁹ I	¹⁴² Pr	¹⁵³ Gd	¹⁶² Er	¹⁶¹ Hf	¹⁷⁰ Os	¹⁸² Au
¹⁰² Sn	¹⁰⁶ Xe	¹³² Nd	¹⁵⁵ Gd	¹⁶³ Er	¹⁶² Hf	¹⁷² Os	¹⁸⁴ Au
¹⁰³ Sn	¹¹⁸ Xe	¹³³ Nd	¹⁴⁷ Tb	¹⁵³ Tm	¹⁶³ Hf	¹⁷³ Os	¹⁸⁵ Au
¹⁰⁴ Sn	¹¹⁹ Xe	¹³⁴ Nd	¹⁴⁸ Tb	¹⁵⁵ Tm	¹⁶⁴ Hf	¹⁷⁴ Os	¹⁸⁹ Au
¹⁰⁵ Sn	¹²⁰ Xe	¹³⁵ Nd	¹⁴⁹ Tb	¹⁵⁸ Tm	¹⁶⁵ Hf	¹⁷⁵ Os	¹⁸⁰ Hg
¹⁰⁶ Sn	¹²¹ Xe	¹³⁶ Nd	¹⁴² Dy	¹⁵⁹ Tm	¹⁶⁶ Hf	¹⁷⁶ Os	¹⁸² Hg
¹⁰⁷ Sn	¹²² Xe	¹³⁷ Nd	¹⁴⁴ Dy	¹⁶¹ Tm	¹⁶⁷ Hf	¹⁷⁷ Os	¹⁸⁴ Hg
¹⁰⁸ Sn	¹²³ Xe	¹³⁸ Nd	¹⁴⁶ Dy	¹⁶³ Tm	¹⁶⁹ Hf	¹⁷⁸ Os	¹⁸⁵ Hg
¹⁰⁹ Sn	¹²¹ Cs	¹³⁹ Nd	¹⁴⁷ Dy	¹⁶⁵ Tm	¹⁷⁰ Hf	¹⁷⁹ Os	¹⁸⁶ Hg
¹¹⁰ Sn	¹²³ Cs	¹⁴² Nd	¹⁴⁸ Dy	¹⁵² Yb	¹⁷¹ Hf	¹⁸⁰ Os	¹⁸⁷ Hg
¹¹¹ Sn	¹²⁵ Cs	¹³¹ Pm	¹⁴⁹ Dy	¹⁵³ Yb	¹⁷² Hf	¹⁸¹ Os	¹⁸⁸ Hg
¹¹² Sn	¹²⁷ Cs	¹³³ Pm	¹⁵⁰ Dy	¹⁵⁴ Yb	¹⁷³ Hf	¹⁸² Os	¹⁸⁹ Hg
¹¹³ Sn	¹²³ Ba	¹³⁷ Pm	¹⁵¹ Dy	¹⁵⁶ Yb	¹⁵⁵ Ta	¹⁸³ Os	¹⁹⁰ Hg
¹¹⁴ Sn	¹²⁴ Ba	¹⁴³ Pm	¹⁵² Dy	¹⁵⁷ Yb	¹⁶⁵ Ta	¹⁸⁷ Os	¹⁹¹ Hg
¹¹⁵ Sn	¹²⁵ Ba	¹³⁴ Sm	¹⁵⁴ Dy	¹⁵⁸ Yb	¹⁶⁷ Ta	¹⁷² Ir	¹⁹² Hg
¹⁰⁵ Sb	¹²⁶ Ba	¹³⁶ Sm	¹⁵⁵ Dy	¹⁵⁹ Yb	¹⁶⁹ Ta	¹⁷⁵ Ir	¹⁹³ Hg
¹⁰⁶ Sb	¹²⁷ Ba	¹³⁷ Sm	¹⁵⁶ Dy	¹⁶⁰ Yb	¹⁵⁸ W	¹⁷⁷ Ir	¹⁹⁴ Hg
¹⁰⁷ Sb	¹²⁸ Ba	¹³⁸ Sm	¹⁵⁷ Dy	¹⁶¹ Yb	¹⁶⁰ W	¹⁷⁹ Ir	¹⁹⁵ Hg
¹⁰⁸ Sb	¹²⁹ Ba	¹³⁹ Sm	¹⁵⁹ Dy	¹⁶² Yb	¹⁶⁴ W	¹⁸¹ Ir	¹⁹⁷ Hg
¹⁰⁹ Sb	¹³⁰ Ba	¹⁴⁰ Sm	¹⁴⁹ Ho	¹⁶³ Yb	¹⁶⁶ W	¹⁸³ Ir	¹⁹⁹ Hg
¹¹¹ Sb	¹³⁸ Ba	¹⁴¹ Sm	¹⁵⁰ Ho	¹⁶⁴ Yb	¹⁶⁷ W	¹⁸⁷ Ir	²⁰¹ Hg
¹¹² Sb	¹²⁹ La	¹⁴² Sm	¹⁵¹ Ho	¹⁶⁵ Yb	¹⁶⁸ W	¹⁶⁸ Pt	²⁰³ Hg
¹¹³ Sb	¹³¹ La	¹⁴³ Sm	¹⁵⁴ Ho	¹⁶⁶ Yb	¹⁶⁹ W	¹⁷⁰ Pt	¹⁸⁷ Tl
¹¹⁵ Sb	¹²⁶ Ce	¹⁴⁴ Sm	¹⁵⁵ Ho	¹⁶⁷ Yb	¹⁷⁰ W	¹⁷⁴ Pt	¹⁸⁹ Tl
¹³³ Sb	¹²⁸ Ce	¹⁴⁵ Sm	¹⁵⁷ Ho	¹⁷¹ Yb	¹⁷¹ W	¹⁷⁶ Pt	¹⁹² Tl
¹⁰² Te	¹²⁹ Ce	¹³⁷ Eu	¹⁵⁹ Ho	¹⁷⁸ Yb	¹⁷² W	¹⁷⁷ Pt	

TABLE II: Targets for (p, γ) reactions with negative Q value but smaller SEF than their inverse reaction. No stable or longlived targets were found.

¹⁸ Ne	³⁹ V	⁵³ Ni	⁷⁶ Sr	¹⁰³ Sn	¹¹⁴ Xe	¹⁵² Yb	¹⁸⁰ Hg
²⁴ Si	⁴⁴ Cr	⁵⁴ Ni	⁸⁶ Ru	¹⁰⁴ Sn	¹²⁶ Nd	¹⁵³ Yb	¹⁸¹ Hg
²⁹ S	⁴³ Mn	⁵¹ Cu	⁸⁸ Ru	¹⁰⁴ Te	¹³⁰ Sm	¹⁵⁴ Hf	¹⁸⁶ Pb
³³ Ar	⁴⁶ Fe	⁵⁶ Zn	⁹⁰ Pd	¹⁰⁶ Te	¹³⁶ Gd	¹⁵⁷ Hf	¹⁸⁸ Pb
³¹ K	⁴⁷ Fe	⁵⁷ Zn	⁹² Pd	¹⁰⁸ Te	¹³⁸ Dy	¹⁵⁸ W	
³⁶ Ca	⁴⁸ Fe	⁵⁸ Zn	⁹⁵ Cd	¹⁰⁹ Te	¹⁴⁴ Dy	¹⁶⁰ W	
³⁷ Ca	⁴⁹ Fe	⁶⁰ Ge	⁹⁶ Cd	¹¹⁰ Te	¹⁴⁸ Er	¹⁶⁴ Os	
³⁸ Ca	⁴⁷ Co	⁶¹ Ge	¹⁰⁰ Sn	¹¹² Xe	¹⁵⁰ Yb	¹⁷⁰ Os	
⁴⁰ Ti	⁵² Ni	⁶² Ge	¹⁰² Sn	¹¹³ Xe	¹⁵¹ Yb	¹⁷⁶ Pt	

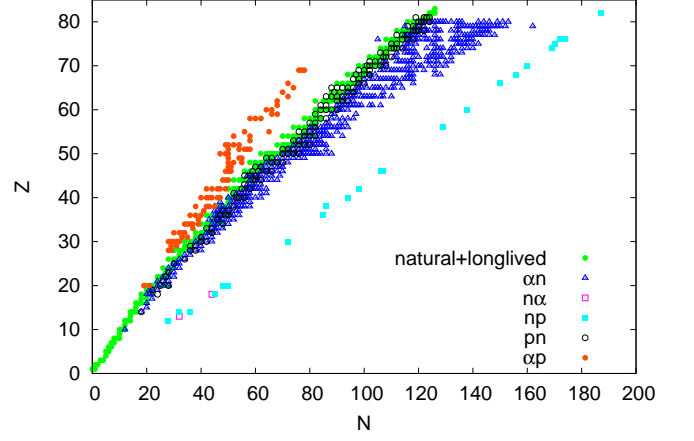


FIG. 4: (Color online) Targets for endothermic reactions with $f_{\text{rev}} < f_{\text{forw}}$ in the nuclear chart, where charge is denoted by Z and neutron number by N . The reaction type is given by the label. Only reactions without γ channels are shown. Also printed for orientation are stable and longlived nuclides.

TABLE III: Targets for (γ, n) reactions with negative Q value but smaller SEF than their inverse reaction. No stable or longlived targets were found.

³⁶ Ne	⁵¹ P	⁷⁰ Ca	¹⁰² Zn	¹²⁵ Y	¹³⁷ Nb	¹⁸⁶ Ce	¹⁸⁸ Nd
³⁴ Na	⁵³ P	⁸² Cr	¹¹⁶ Se	¹³¹ Y	¹³⁰ Mo	¹⁸⁸ Ce	¹⁹⁴ Nd
⁴² Mg	⁵⁵ P	⁸³ Mn	¹²¹ Rb	¹²⁶ Zr	¹⁴⁰ Mo	¹⁸⁷ Pr	²³⁶ Hf
⁴⁰ Al	⁵⁸ S	⁹⁰ Fe	¹²² Sr	¹³⁰ Zr	¹⁵¹ Rh	¹⁸⁹ Pr	²⁴⁶ Os
⁵⁰ Si	⁶⁴ Ar	⁹⁴ Ni	¹²⁸ Sr	¹²⁹ Nb	¹⁵² Pd	¹⁹³ Pr	¹⁷⁶ Au

integrations, it becomes obvious that even for α captures with negative Q value the SEF of the capture reaction is smaller than the one of the photodisintegration. Thus, a measurement of the capture includes more astrophysically relevant transitions and is closer to the stellar value than a measurement of the photodisintegration in the laboratory. Many of the cases with negative Q value are found at stability, providing interesting examples for experimental study. A second class of interesting reactions are the (p, γ) and (γ, p) reactions in Fig. 3 and Tables II, IV. They involve unstable targets and are of interest in the rp process [15] and the νp process [16].

Figure 4 displays reactions without a photon channel.

TABLE IV: Targets for (γ, p) , (n, α) , and (n, γ) reactions with negative Q value but smaller SEF than their inverse reaction. No stable or longlived targets were found.

(γ, p) :		
	²⁸ Ar	⁴⁷ Mn ¹⁷⁶ Au
(n, α) :		
	⁴⁵ Al	⁶² Ar
(n, γ) :		
	⁸³ Cr	¹³² Pd ¹³⁶ Cd

TABLE V: Targets for (p,n) reactions with negative Q value but smaller SEF than their inverse reaction. Stable or longlived targets are in italics.

³² Si	⁷⁷ As	¹⁰¹ Rh	¹²³ Sb	¹⁴⁴ Nd	¹⁵⁹ Tb	¹⁷⁷ Lu	¹⁹⁷ Pt
⁴² Ar	⁸² Se	¹⁰³ Rh	¹²⁵ Sb	¹⁴⁶ Nd	¹⁶¹ Tb	¹⁷⁹ Hf	¹⁹⁸ Pt
⁴¹ K	⁸¹ Br	¹⁰⁵ Rh	¹²⁸ Te	¹⁴⁸ Nd	¹⁶⁴ Dy	¹⁸⁰ Hf	²⁰⁰ Pt
⁴⁵ Ca	⁸³ Kr	¹⁰⁵ Pd	¹³⁰ Te	¹⁵⁰ Nd	¹⁶⁶ Dy	¹⁸² Hf	¹⁹⁵ Au
⁴⁸ Ca	⁸⁵ Kr	¹⁰⁷ Pd	¹³² Te	¹⁴⁵ Pm	¹⁶³ Ho	¹⁷⁹ Ta	¹⁹⁷ Au
⁴⁷ Sc	⁸⁶ Kr	¹¹⁰ Pd	¹²⁷ I	¹⁴⁷ Pm	¹⁶⁵ Ho	¹⁸¹ Ta	¹⁹⁹ Au
⁴⁹ Ti	⁸⁵ Rb	¹¹² Pd	¹²⁹ I	¹⁵² Sm	¹⁶⁵ Er	¹⁸⁴ W	²⁰⁰ Hg
⁵¹ V	⁸⁷ Rb	¹⁰⁷ Ag	¹³² Xe	¹⁵⁴ Sm	¹⁶⁸ Er	¹⁸⁵ W	²⁰¹ Hg
⁵⁵ Mn	⁹⁰ Sr	¹⁰⁹ Ag	¹³⁴ Xe	¹⁵⁶ Sm	¹⁷⁰ Er	¹⁸⁶ W	²⁰² Hg
⁶⁰ Fe	⁹³ Zr	¹¹⁴ Cd	¹³⁶ Xe	¹⁴⁹ Eu	¹⁶⁷ Tm	¹⁸⁸ W	²⁰⁴ Hg
⁶⁴ Ni	⁹⁴ Zr	¹¹⁶ Cd	¹³¹ Cs	¹⁵¹ Eu	¹⁶⁹ Tm	¹⁸⁵ Re	²⁰⁰ Tl
⁶⁶ Ni	⁹⁶ Zr	¹¹⁸ Cd	¹³³ Cs	¹⁵³ Eu	¹⁷¹ Tm	¹⁸⁷ Re	²⁰³ Tl
⁶⁵ Cu	⁹³ Nb	¹¹³ In	¹³⁵ Cs	¹⁵⁵ Eu	¹⁷¹ Yb	¹⁹⁰ Os	²⁰⁴ Tl
⁶⁷ Cu	⁹⁷ Mo	¹¹⁵ In	¹³⁸ Ba	¹⁵³ Gd	¹⁷² Yb	¹⁹² Os	²⁰⁵ Tl
⁷⁰ Zn	¹⁰⁰ Mo	¹²⁰ Sn	¹³⁷ La	¹⁵⁸ Gd	¹⁷⁴ Yb	¹⁹⁴ Os	
⁷² Zn	⁹⁹ Tc	¹²² Sn	¹³⁹ La	¹⁶⁰ Gd	¹⁷⁶ Yb	¹⁸⁹ Ir	
⁷¹ Ga	¹⁰³ Ru	¹²⁴ Sn	¹⁴² Ce	¹⁵³ Tb	¹⁷⁸ Yb	¹⁹¹ Ir	
⁷⁶ Ge	¹⁰⁴ Ru	¹²⁶ Sn	¹⁴⁴ Ce	¹⁵⁵ Tb	¹⁷³ Lu	¹⁹³ Ir	
⁷⁵ As	¹⁰⁶ Ru	¹²¹ Sb	¹⁴¹ Pr	¹⁵⁷ Tb	¹⁷⁵ Lu	¹⁹⁶ Pt	

TABLE VI: Targets for (n,p) reactions with negative Q value but smaller SEF than their inverse reaction. No stable or longlived targets were found.

⁴⁰ Mg	⁶³ Ar	¹⁰² Zn	¹³⁴ Zr	¹⁵³ Pd	²¹⁶ Dy	²⁴³ W	²⁵⁰ Os
⁴⁶ Si	⁶⁸ Ca	¹²¹ Kr	¹⁴⁰ Mo	¹⁸⁵ Ba	²²⁴ Er	²⁴⁵ Re	²⁶⁹ Pb
⁵⁰ Si	⁷⁰ Ca	¹²⁴ Sr	¹⁵² Pd	¹⁹⁸ Nd	²³⁰ Yb	²⁴⁸ Os	

Mostly interesting is the large number of (p,n) reactions located along stability (see Table V). A recent investigation of the γ process has pointed out the importance of (n,p) reactions close to stability [6]. According to our findings, it is best to study the endothermic (p,n) reaction when trying to experimentally constrain the astrophysical rate. Our measurement of ⁸⁵Rb(p,n)⁸⁵Sr, described in the following section, is an example for such an experiment.

Of minor or no astrophysical relevance are the (α ,n) and (n,p) reactions in Fig. 4 and Tables VII, VI because they involve neutron-rich targets and these reactions are much slower than other possible reactions on the same nuclei.

Figure 3 and Tables III, IV list (n, γ) and (γ ,n) reactions on very neutron-rich nuclei far off stability. They are relevant in the r process [17, 18]. Obviously, the suppression of the SEF is not caused by the Coulomb barrier. The nuclear structure (spins and parities of excited states and the nuclear level density) is important in those cases, as the level density is low and transitions are favored or suppressed by selection rules and centrifugal barriers. Contrary to the Coulomb suppression of the SEF, this type of suppression is strongly dependent on the nuclear spectroscopy assumed in the calculation.

TABLE VII: Targets for (α ,n) reactions with negative Q value but smaller SEF than their inverse reaction. Stable or longlived targets are in italics.

²² Ne	⁸³ Kr	¹⁰⁶ Ru	¹³³ Te	¹⁶⁰ Pm	¹⁷⁵ Tm	¹⁹⁰ W	¹⁹⁸ Pt
³² Si	⁸⁴ Kr	¹⁰⁸ Ru	¹³⁴ Te	¹⁶³ Pm	¹⁷⁶ Tm	¹⁹² W	¹⁹⁹ Pt
³⁵ P	⁸⁶ Kr	¹¹⁰ Ru	¹³⁵ Te	¹⁶⁴ Pm	¹⁷⁸ Tm	¹⁹⁷ W	²⁰⁰ Pt
³⁶ S	⁸⁷ Kr	¹¹² Ru	¹³⁶ Te	¹⁶⁷ Pm	¹⁷⁹ Tm	²⁰⁰ W	²⁰¹ Pt
³⁹ Cl	⁸⁸ Kr	¹⁰² Rh	¹³⁷ Te	¹⁵⁴ Sm	¹⁸⁰ Tm	²⁰¹ W	²⁰² Pt
³⁸ Ar	⁹⁰ Kr	¹⁰³ Rh	¹³⁸ Te	¹⁵⁶ Sm	¹⁸¹ Tm	²⁰² W	²⁰⁴ Pt
³⁹ Ar	⁸² Rb	¹⁰⁴ Rh	¹²⁹ I	¹⁵⁸ Sm	¹⁸² Tm	²⁰³ W	²⁰⁵ Pt
⁴⁰ Ar	⁸³ Rb	¹⁰⁵ Rh	¹³¹ I	¹⁵⁵ Eu	¹⁸³ Tm	²⁰⁶ W	²⁰⁶ Pt
⁴⁰ K	⁸⁴ Rb	¹⁰⁶ Rh	¹³² I	¹⁵⁷ Eu	¹⁸⁴ Tm	²⁰⁷ W	²¹⁰ Pt
⁴¹ K	⁸⁵ Rb	¹⁰⁷ Rh	¹³³ I	¹⁵⁸ Eu	¹⁸⁵ Tm	²¹⁰ W	²¹² Pt
⁴³ K	⁸⁶ Rb	¹⁰⁹ Rh	¹³⁵ I	¹⁵⁹ Eu	¹⁸⁶ Tm	²¹² W	²¹³ Pt
⁴⁴ Ca	⁸⁷ Rb	¹¹¹ Rh	¹³⁶ I	¹⁶⁰ Eu	¹⁸⁸ Tm	²¹⁴ W	²¹⁸ Pt
⁴⁶ Ca	⁸⁸ Rb	¹¹⁴ Rh	¹³⁷ I	¹⁶² Eu	¹⁹¹ Tm	¹⁹⁰ Re	²²⁰ Pt
⁴⁸ Ca	⁹⁰ Rb	¹⁰⁸ Pd	¹³² Xe	¹⁶³ Eu	¹⁹⁵ Tm	¹⁹¹ Re	²²¹ Pt
⁴⁵ Sc	⁹¹ Rb	¹⁰⁹ Pd	¹³⁴ Xe	¹⁶⁴ Eu	¹⁷⁷ Yb	¹⁹² Re	²²² Pt
⁴⁷ Sc	⁸³ Sr	¹¹⁰ Pd	¹³⁶ Xe	¹⁶⁵ Eu	¹⁷⁸ Yb	¹⁹⁴ Re	²²³ Pt
⁴⁹ Sc	⁸⁵ Sr	¹¹¹ Pd	¹³⁸ Xe	¹⁶⁶ Eu	¹⁸⁶ Yb	²⁰⁰ Re	²²⁴ Pt
⁴⁸ Ti	⁸⁶ Sr	¹¹² Pd	¹³⁹ Xe	¹⁶⁷ Eu	¹⁸⁸ Yb	²⁰¹ Re	¹⁹⁴ Au
⁵⁰ Ti	⁸⁸ Sr	¹¹⁴ Pd	¹⁴⁰ Xe	¹⁶⁹ Eu	¹⁹⁰ Yb	²⁰⁹ Re	¹⁹⁸ Au
⁵² Ti	⁹⁰ Sr	¹¹⁶ Pd	¹⁴¹ Xe	¹⁷⁰ Eu	¹⁹¹ Yb	²¹⁰ Re	¹⁹⁹ Au
⁵¹ V	⁹¹ Sr	¹⁰⁹ Ag	¹⁴² Xe	¹⁷³ Eu	¹⁹⁴ Yb	²¹¹ Re	²⁰¹ Au
⁵³ V	⁹² Sr	¹¹¹ Ag	¹⁴⁶ Xe	¹⁵⁸ Gd	¹⁹⁶ Yb	²¹² Re	²⁰⁵ Au
⁵² Cr	⁹³ Sr	¹¹³ Ag	¹³⁵ Cs	¹⁶⁰ Gd	¹⁹⁸ Yb	²¹³ Re	²¹³ Au
⁵⁴ Cr	⁹⁴ Sr	¹¹⁵ Ag	¹³⁷ Cs	¹⁶¹ Gd	²⁰⁰ Yb	²¹⁵ Re	²¹⁴ Au
⁵⁶ Cr	⁹⁶ Sr	¹¹⁶ Ag	¹³⁸ Cs	¹⁶² Gd	¹⁷⁸ Lu	²¹⁷ Re	²¹⁵ Au
⁵⁵ Mn	⁸⁶ Y	¹¹⁷ Ag	¹³⁹ Cs	¹⁷¹ Gd	¹⁷⁹ Lu	¹⁸¹ Os	²¹⁶ Au
⁵⁶ Mn	⁹⁰ Y	¹¹² Cd	¹⁴⁰ Cs	¹⁶² Tb	¹⁸³ Lu	¹⁹² Os	²¹⁷ Au
⁵⁷ Mn	⁹¹ Y	¹¹⁴ Cd	¹⁴¹ Cs	¹⁶³ Tb	¹⁸⁴ Lu	¹⁹³ Os	²¹⁸ Au
⁵⁸ Fe	⁹² Y	¹¹⁶ Cd	¹⁴⁵ Cs	¹⁶⁴ Tb	¹⁸⁵ Lu	¹⁹⁴ Os	²¹⁹ Au
⁶⁰ Fe	⁹³ Y	¹¹⁸ Cd	¹³⁶ Ba	¹⁶⁶ Tb	¹⁸⁶ Lu	¹⁹⁵ Os	²²⁰ Au
⁶¹ Co	⁹⁴ Y	¹²⁰ Cd	¹³⁸ Ba	¹⁶⁸ Tb	¹⁸⁷ Lu	¹⁹⁶ Os	²²¹ Au
⁶³ Co	⁹⁵ Y	¹¹⁷ In	¹⁴⁰ Ba	¹⁶⁹ Tb	¹⁸⁸ Lu	¹⁹⁸ Os	²²² Au
⁶⁴ Ni	⁹⁷ Y	¹¹⁹ In	¹⁴¹ Ba	¹⁷⁰ Tb	¹⁸⁹ Lu	¹⁹⁹ Os	²²³ Au
⁶⁶ Ni	⁹⁰ Zr	¹²¹ In	¹⁴² Ba	¹⁷¹ Tb	¹⁹⁴ Lu	²⁰⁰ Os	²²⁴ Au
⁶⁸ Ni	⁹² Zr	¹²³ In	¹⁴³ Ba	¹⁷³ Tb	¹⁹⁵ Lu	²⁰² Os	²²⁵ Au
⁶⁷ Cu	⁹⁴ Zr	¹²⁵ In	¹⁴⁴ Ba	¹⁷⁵ Tb	¹⁹⁷ Lu	²⁰³ Os	²²⁶ Au
⁶⁹ Cu	⁹⁵ Zr	¹²⁷ In	¹⁴⁵ Ba	¹⁷⁶ Tb	¹⁹⁸ Lu	²⁰⁴ Os	²²⁷ Au
⁶⁸ Zn	⁹⁶ Zr	¹²⁰ Sn	¹⁴⁶ Ba	¹⁷⁹ Tb	²⁰¹ Lu	²⁰⁸ Os	²²⁸ Au
⁷⁰ Zn	⁹⁷ Zr	¹²² Sn	¹⁴⁷ Ba	¹⁶⁴ Dy	²⁰³ Lu	²⁰⁹ Os	²²⁹ Au
⁷² Zn	⁹⁸ Zr	¹²⁴ Sn	¹⁴⁸ Ba	¹⁶⁶ Dy	¹⁸³ Hf	²¹⁰ Os	²³¹ Au
⁷⁴ Zn	¹⁰⁰ Zr	¹²⁵ Sn	¹⁵⁰ Ba	¹⁷⁷ Dy	¹⁸⁴ Hf	²¹¹ Os	²⁴¹ Au
⁷¹ Ga	¹⁰² Zr	¹²⁶ Sn	¹⁴³ La	¹⁷⁹ Dy	¹⁹⁰ Hf	²¹³ Os	²⁰¹ Hg
⁷³ Ga	⁹⁴ Nb	¹²⁷ Sn	¹⁴⁴ La	¹⁸⁴ Dy	¹⁹² Hf	²¹⁴ Os	²⁰² Hg
⁷⁵ Ga	⁹⁵ Nb	¹²⁸ Sn	¹⁴⁸ La	¹⁶⁷ Ho	¹⁹⁵ Hf	²¹⁵ Os	²⁰⁴ Hg
⁷⁴ Ge	⁹⁶ Nb	¹²⁹ Sn	¹⁵⁰ La	¹⁶⁹ Ho	¹⁹⁶ Hf	²¹⁶ Os	²⁰⁵ Hg
⁷⁵ Ge	⁹⁷ Nb	¹³⁰ Sn	¹⁴⁶ Ce	¹⁷⁰ Ho	¹⁹⁷ Hf	¹⁹² Ir	²⁰⁶ Hg
⁷⁶ Ge	⁹⁸ Nb	¹³¹ Sn	¹⁴⁸ Ce	¹⁷² Ho	¹⁹⁸ Hf	¹⁹³ Ir	²⁰⁷ Hg
⁷⁸ Ge	⁹⁹ Nb	¹³² Sn	¹⁵⁰ Ce	¹⁷³ Ho	¹⁹⁹ Hf	¹⁹⁴ Ir	²⁰⁸ Hg
⁷⁷ As	¹⁰³ Nb	¹³³ Sn	¹⁵² Ce	¹⁷⁴ Ho	²⁰⁰ Hf	¹⁹⁵ Ir	²⁰⁹ Hg
⁷⁸ As	¹⁰⁵ Nb	¹³⁴ Sn	¹⁵⁴ Ce	¹⁷⁵ Ho	²⁰¹ Hf	¹⁹⁶ Ir	²¹⁰ Hg
⁷⁹ As	⁹⁸ Mo	¹³⁶ Sn	¹⁴⁷ Pr	¹⁷⁶ Ho	²⁰⁴ Hf	¹⁹⁷ Ir	²¹² Hg
⁸¹ As	⁹⁹ Mo	¹³⁸ Sn	¹⁴⁸ Pr	¹⁷⁷ Ho	¹⁸⁵ Ta	¹⁹⁹ Ir	²¹⁴ Hg
⁷⁸ Se	¹⁰⁰ Mo	¹²³ Sb	¹⁵⁶ Pr	¹⁷⁸ Ho	¹⁸⁸ Ta	²⁰³ Ir	²¹⁵ Hg
⁷⁹ Se	¹⁰¹ Mo	¹²⁵ Sb	¹⁵⁰ Nd	¹⁷⁹ Ho	¹⁸⁹ Ta	²¹¹ Ir	²¹⁶ Hg
⁸⁰ Se	¹⁰² Mo	¹²⁷ Sb	¹⁵¹ Nd	¹⁸¹ Ho	¹⁹⁰ Ta	²¹³ Ir	²²² Hg
⁸² Se	¹⁰³ Mo	¹²⁸ Sb	¹⁵² Nd	¹⁸² Ho	¹⁹¹ Ta	²¹⁴ Ir	²²⁴ Hg
⁸⁴ Se	¹⁰⁴ Mo	¹²⁹ Sb	¹⁵⁴ Nd	¹⁸³ Ho	¹⁹² Ta	²¹⁵ Ir	²²⁶ Hg
⁷⁸ Br	¹⁰⁶ Mo	¹³⁰ Sb	¹⁵¹ Pm	¹⁸⁴ Ho	¹⁹⁸ Ta	²¹⁶ Ir	²²⁹ Hg
⁸⁰ Br	¹⁰⁰ Tc	¹³¹ Sb	¹⁵² Pm	¹⁸⁵ Ho	¹⁹⁹ Ta	²¹⁷ Ir	²³¹ Hg
⁸¹ Br	¹⁰¹ Tc	¹³³ Sb	¹⁵³ Pm	¹⁷⁰ Er	²⁰¹ Ta	²¹⁸ Ir	²³³ Hg
⁸² Br	¹⁰² Tc	¹³⁷ Sb	¹⁵⁴ Pm	¹⁷² Er	²⁰⁴ Ta	²¹⁹ Ir	
⁸³ Br	¹⁰³ Tc	¹²⁶ Te	¹⁵⁵ Pm	¹⁸⁴ Er	²⁰⁵ Ta	²²⁰ Ir	
⁸⁵ Br	¹⁰⁵ Tc	¹²⁸ Te	¹⁵⁶ Pm	¹⁸⁵ Er	²⁰⁷ Ta	²²¹ Ir	
⁸⁷ Br	¹⁰² Ru	¹³⁰ Te	¹⁵⁷ Pm	¹⁸⁶ Er	²⁰⁹ Ta	²²³ Ir	
⁸¹ Kr	¹⁰⁴ Ru	¹³¹ Te	¹⁵⁸ Pm	¹⁹⁴ Er	¹⁸⁸ W	²²⁵ Ir	
⁸² Kr	¹⁰⁵ Ru	¹³² Te	¹⁵⁹ Pm	¹⁹⁶ Er	¹⁸⁹ W	¹⁹⁶ Pt	

TABLE VIII: Targets for (α, p) reactions with negative Q value but smaller SEF than their inverse reaction. Stable or longlived targets are in italics.

³⁹ Ca	⁶⁶ Ga	⁷² Kr	⁸⁶ Zr	⁹⁷ Pd	¹⁰¹ Sb	¹¹¹ Cs	¹³⁴ Gd
⁴¹ <i>Ca</i>	⁶² Ge	⁷⁴ Kr	⁸⁷ Zr	⁹⁷ Ag	¹⁰⁵ Sb	¹²⁰ Cs	¹³⁹ Tb
⁵⁶ Ni	⁶⁴ Ge	⁷⁶ Kr	⁸⁴ Mo	⁹⁸ Ag	¹⁰⁷ Sb	¹¹⁶ Ce	¹³⁸ Dy
⁵⁷ Ni	⁶⁵ Ge	⁷⁸ Rb	⁸⁶ Mo	⁹⁸ Cd	¹⁰⁸ Sb	¹¹⁸ Ce	¹⁴⁵ Tm
⁵⁸ Cu	⁶⁶ Ge	⁷⁶ Sr	⁸⁸ Mo	¹⁰⁰ Cd	¹⁰⁹ Sb	¹²⁰ Ce	¹⁴⁶ Tm
⁶⁰ Cu	⁷⁰ As	⁸⁰ Sr	⁸⁹ Mo	¹⁰³ Cd	¹⁰¹ Te	¹²⁵ Pr	¹⁴⁷ Tm
⁵⁸ Zn	⁶⁸ Se	⁸¹ Sr	⁹¹ Mo	⁹⁹ In	¹⁰² Te	¹²⁷ Pr	
⁵⁹ Zn	⁶⁹ Se	⁸³ Sr	⁹² Ru	¹⁰³ In	¹⁰⁴ Te	¹²⁴ Nd	
⁶⁰ Zn	⁷⁰ Se	⁸⁰ Zr	⁹³ Ru	¹⁰⁴ In	¹⁰⁶ Te	¹²⁶ Nd	
⁶¹ Zn	⁷¹ Se	⁸² Zr	⁹⁴ Ru	⁹⁷ Sn	¹¹¹ I	¹²⁹ Pm	
⁶² Zn	⁷³ Se	⁸³ Zr	⁹⁵ Pd	⁹⁹ Sn	¹⁰⁶ Xe	¹³⁰ Sm	
⁶⁴ Ga	⁷⁴ Br	⁸⁴ Zr	⁹⁶ Pd	¹⁰⁰ Sn	¹¹² Xe	¹³⁵ Eu	

Moreover, the Hauser-Feshbach model of compound reactions may not be applicable anymore for the nuclei involved [19]. Additionally, the individual rates are not important in r process studies producing highly unstable, neutron-rich nuclei close to the dripline in an equilibrium between capture and photodisintegration [20, 21].

III. EXPERIMENTAL STUDY OF $^{85}\text{Rb}(p, n)^{85}\text{Sr}$

A. General

As an example of the suppression effect and for the derivation of the astrophysical rates for an endothermic reaction, we experimentally studied the reaction $^{85}\text{Rb}(p, n)^{85}\text{Sr}$.

Reactions of the (n, p) type have been shown to be important in the γ process [6]. This nucleosynthesis process creates proton-rich isotopes of elements beyond Fe which are not made in the s and r processes. It was shown to occur in hot O/Ne layers of massive stars, either in a core collapse supernova explosion when the shockfront is passing these layers or already pre-explosively depending on the initial mass of the star [4]. At temperatures $T > 2$ GK photodisintegrations can act even within the short timescale of an explosion. The reaction sequences initially drive material from the bottom of the valley of stability to the proton-rich side by (γ, n) reactions. Charged-particle emitting (γ, α) and (γ, p) reactions can deflect the reaction path to lower charge number. Theoretical investigations show that $(\gamma, n)/(\gamma, p)$ branchings play a key role in the production of the lighter p nuclei whereas $(\gamma, n)/(\gamma, \alpha)$ branchings are important at higher masses [5, 6]. Further reactions with the emitted neutrons are mainly important in the freeze-out phase when photodisintegration ceases [6, 22]. The flow back to stability is sped up by (n, p) reactions which are faster than β decays close to stability [6]. Even at stability, (n, p) reactions act to push material to lower proton numbers. In this context, $^{85}\text{Rb}(p, n)^{85}\text{Sr}$ is directly important because

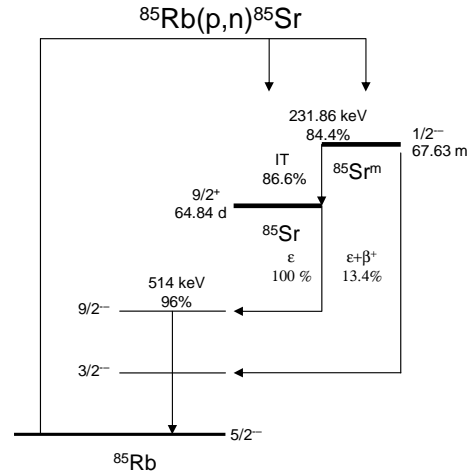


FIG. 5: Simplified decay scheme of the products of the $^{85}\text{Rb}(p, n)^{85}\text{Sr}$ reaction. The half-lives of the reaction products, the branching ratios, the spin and parity of the levels and the transitions used to determine the reaction cross section are indicated [23].

it is the inverse reaction to $^{85}\text{Sr}(n, p)$ and we found that its SEF is smaller than the one of its inverse, despite of its negative Q value (see Sec. III G).

The reaction $^{85}\text{Rb}(p, n)^{85}\text{Sr}$ is also important to test the predictions of astrophysical rates and their underlying nuclear properties. Although many (n, p) and (p, γ) reactions important in the γ , rp , and νp processes [6, 15, 16] occur far from stability, the models and assumptions used in the prediction of the rates can be checked at stability. Especially suited for testing the reliability of the optical potential used for the calculation of transitions involving protons are (n, p) and (p, n) reactions because the proton width is smaller than the neutron width at practically all energies (except very close to the neutron threshold) and thus determines the cross section.

We measured $^{85}\text{Rb}(p, n)^{85}\text{Sr}$ using the activation method. Thin RbCl targets were bombarded by proton beam provided by the Van de Graaff and cyclotron accelerators of ATOMKI [7]. The (p, n) reaction on ^{85}Rb can populate both the ground and metastable states of ^{85}Sr [23]. To determine the cross section of the $^{85}\text{Rb}(p, n)^{85}\text{Sr}^g$ reaction the 514.01 keV γ line was used, in the case of the $^{85}\text{Rb}(p, n)^{85}\text{Sr}^m$ reaction cross section the yield of the 231.84 keV transition was measured. In the following Secs. III B–III D a detailed description of the experimental technique is given, while the experimental results are given in Sec. III E. A comparison to theory and the final astrophysical reaction rates are provided in Secs. III F and III G.

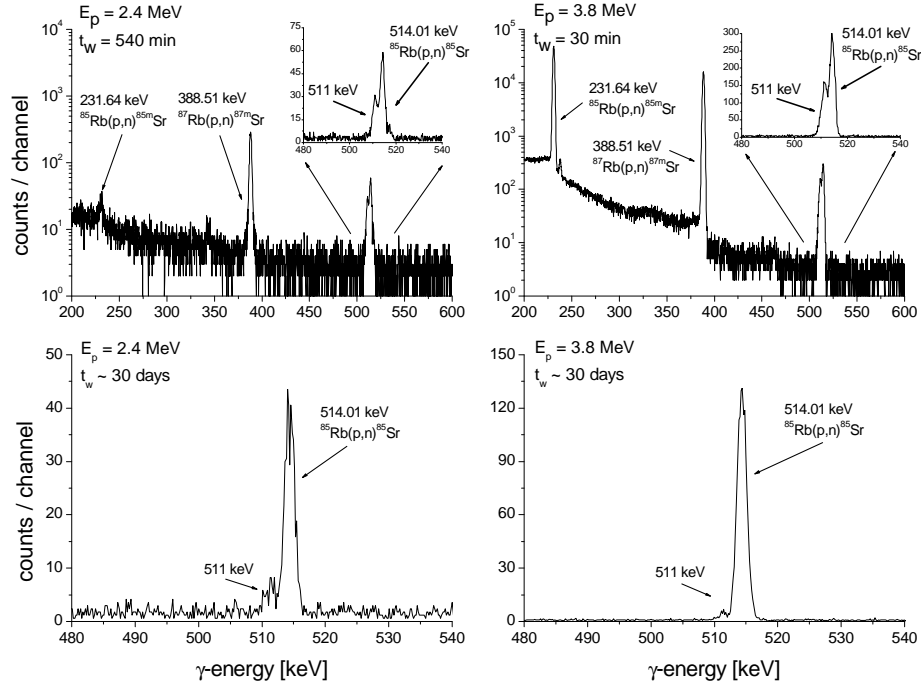


FIG. 6: Typical γ -spectra taken after the irradiation of RbCl targets with 2.4 (left panel) and 3.8 MeV (right panel) proton beams. The 514.01 keV peak from the $^{85}\text{Rb}(p,n)^{85}\text{Sr}^g$ reaction can be well separated from the annihilation peak as can be seen in the insets. The length of the waiting time (t_w) between the end of the irradiation and the start of the γ -countings were 540 ($E_p = 2.4$ MeV) and 30 min ($E_p = 3.8$ MeV). The lower panels show typical spectra taken in the repeated activity measurement approximately one month after the irradiations (for details see text).

B. Target properties and the determination of the number of target atoms

The targets were made by evaporating chemically pure (99.99%) RbCl onto two different kinds of Aluminum foils: the thicker one had a chemical purity of 99.999% and thickness of 50 μm , while the purity and the thickness of the thinner one was 99% and 2.4 μm , respectively. The distance between the evaporation boat and the target backing was 10 cm, therefore it was possible to assume that the evaporated layer is homogeneous. This assumption was proved using Rutherford Backscattering Spectroscopy (RBS, see later). Targets with different thicknesses were used, thicker ones (on thicker backings) were employed for irradiations at lower and thinner ones (on thinner backing) at higher energy. Owing to this treatment, the yield of the investigated 514.01 keV peak was always higher than, or comparable to that of the 511 keV annihilation peak – and this way the separation of the peaks was achieved – as it is demonstrated in the upper part of Fig. 6.

The number of the target atoms was determined with Rutherford Backscattering Spectrometry (RBS) at the Nuclear Microprobe facility of ATOMKI [25, 26, 27]. As a consistency check, in the case of the targets evaporated onto the thinner backing, weighing was also used to determine the number of target atoms. The weight of the Al foil used as backing was measured before and after the

evaporation and from the difference — assuming that our target is uniform — the number of target atoms was calculated. The results of the two different methods used to determine the number of target atoms are in very good agreement ($\leq 3\%$ difference).

C. Irradiation

The RbCl targets were bombarded with a proton beam provided by the Van de Graaff and cyclotron accelerators of ATOMKI. The energy of the proton beam was between 2 and 4 MeV, this energy range was covered in 200 keV steps. The beam current was typically 600 nA. Each irradiation lasted approximately 7 – 8 hours. The low energy irradiations (2.2 MeV, 2.4 MeV and 2.6 MeV) have been carried out using the Van de Graaff. At and above 2.6 MeV the cyclotron accelerator was used. The cross section at $E_p = 2.6$ MeV was measured with both accelerators and no difference was found.

An ion implanted Si detector was built into the irradiation chamber at $\theta = 150^\circ$ relative to the beam direction to measure the yield of the backscattered protons. The backscattering spectra were taken continuously and were used to monitor the target stability. Having a beam restricted to 600 nA, no target deterioration was found.

For calculating the reaction cross section the proper knowledge of the incident particle flux is necessary. To

obtain this, the collected charge was measured in a chamber similar to the one in [1]. After the beam defining aperture, the whole chamber served as Faraday cup to collect the accumulated charge. A secondary electron suppression voltage of -300 V was applied at the entrance of the chamber. The beam current was kept as stable as possible but to follow the changes the current integrator counts were recorded in multichannel scaling mode, stepping the channel in every minute. This recorded current integrator spectrum was used for the analysis solving the differential equation of the population and decay of the reaction products numerically.

D. Activity determination

Figure 5 shows the simplified decay scheme of the $^{85}\text{Sr}^{g,m}$ isotopes. To determine the cross section of the $^{85}\text{Rb}(p,n)^{85}\text{Sr}^g$ reaction the 514.01 keV, for the $^{85}\text{Rb}(p,n)^{85}\text{Sr}^m$ reaction the 231.84 keV gamma line was used.

For measuring the induced γ -activity a lead shielded HPGe detector was used as in our previous (p,n)-study [1]. After each irradiation, a cooling time of one hour was inserted in order to let the disturbing shortlived activities decay. The γ spectra were taken for 12 hours and stored regularly in order to follow the decay of the short-lived reaction product.

Figure 6 shows typical spectra collected after irradiating RbCl targets with the 2.4 MeV (left panel) and the 3.8 MeV (right panel) proton beams. The yield of the 511 keV peak was always less than or comparable to the investigated 514.01 keV transition, as shown in the insets. The ^{85}gSr has a relatively long halflife ($T_{1/2} = 64.84$ d). Due to this, the activity measurement could be repeated for each target after approximately one month, when the intensity of the 511 keV radiation was substantially reduced. The spectra taken in the repeated activity measurement for the 2.4 and 3.8 MeV irradiations are shown in the lower panels of Fig. 6. The two measurements yielded consistent cross sections proving the proper separation of the 511 keV and 514.01 keV peaks.

E. Experimental results and comparison with literature data

In the case of the $^{85}\text{Rb}(p,n)^{85}\text{Sr}^g$ reaction, two separated analysis were done. The agreement between the cross sections derived in the γ -counting after the irradiation and the ones from the repeated activity measurement was always better than 4%. The final results were calculated from the average weighted by the statistical uncertainty of the two γ countings. The halflife of the $^{85}\text{Sr}^m$ is shorter, therefore the yield of the 231.64 keV γ radiation was measured only after the irradiation. The final experimental result can be found in Table IX. Partial cross sections leading to the ground and isomeric state of

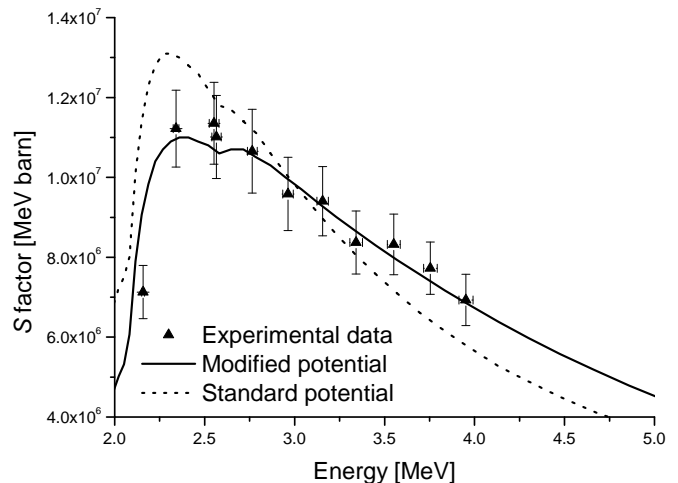


FIG. 7: Experimental (full triangles) and theoretical (lines) astrophysical S factors of $^{85}\text{Rb}(p,n)^{85}\text{Sr}$. The solid line is the S factor calculated with the modified proton optical potential introduced in [1] and the dashed line shows the result using the standard proton optical potential from [31] with low energy modifications by [32] (see text).

^{85}Sr can be found in [7]. The error of the cross section values is the quadratic sum of the following partial errors: efficiency of the HPGe detector system (6%), number of target atoms ($\leq 3.3\%$), current measurement (3%), uncertainty of the level parameters found in the literature ($\leq 4\%$) and counting statistics ($\leq 4\%$). The quoted errors of the energies include the energy loss in the targets calculated with the SRIM code [30], as well as the energy stability of the cyclotron and Van de Graaff accelerators.

The measured total cross sections cover 3 orders of magnitude, varying from 0.06 to 20 mb. Table IX lists the measured cross sections σ and the S factors, the latter being defined as [8]

$$S(E) = \frac{\sigma}{E} e^{-2\pi\eta} \quad , \quad (12)$$

with the Sommerfeld parameter η accounting for the Coulomb barrier penetration.

The cross section of the $^{85}\text{Rb}(p,n)^{85}\text{Sr}$ reaction was already investigated by [24] between $E_{c.m.} = 3.1$ and 70.6 MeV. However, their accuracy is not sufficient for astrophysical applications, mainly because of the large uncertainty of the c.m. energies. Moreover, there is only one data point in the relevant energy region for the γ process and it bears an uncertainty of ± 0.5 MeV in the c.m. energy.

F. Comparison to theory and implications for the proton optical potential

The measured S factors are compared to theoretical predictions obtained with the code NON-SMOKER [11, 14] in Fig. 7. The standard calculation applied a pro-

TABLE IX: Details of the irradiations and the resulted cross sections (astrophysical S factors).

$E_{lab.}$ [MeV]	$E_{c.m.}$ [MeV]	Accelerator	Collected charge [mC]	Total σ [mbarn]	S factor [10^6 MeVbarn]
2.20	2.16 ± 0.008	Van de Graaff	48.27	0.058 ± 0.006	7.13 ± 0.67
2.40	2.34 ± 0.016	Van de Graaff	37.23	0.224 ± 0.019	11.22 ± 0.96
2.60	2.57 ± 0.026	Van de Graaff	33.74	0.582 ± 0.055	11.01 ± 1.04
2.58	2.55 ± 0.027	Cyclotron	35.44	0.569 ± 0.051	11.35 ± 1.02
2.79	2.77 ± 0.028	Cyclotron	30.83	1.20 ± 0.12	10.65 ± 1.05
2.98	2.96 ± 0.030	Cyclotron	23.66	2.12 ± 0.21	9.59 ± 0.92
3.18	3.16 ± 0.032	Cyclotron	23.43	3.77 ± 0.35	9.40 ± 0.87
3.37	3.34 ± 0.035	Cyclotron	21.45	5.66 ± 0.54	8.37 ± 0.79
3.57	3.55 ± 0.036	Cyclotron	20.64	9.60 ± 0.87	8.32 ± 0.76
3.76	3.75 ± 0.037	Cyclotron	17.16	14.31 ± 1.22	7.73 ± 0.66
3.96	3.95 ± 0.040	Cyclotron	11.51	19.65 ± 1.82	6.93 ± 0.64

ton optical potential widely used in astrophysical applications, based on a microscopic approach utilizing a local density approximation [31]. Low-energy modifications, which are relevant in astrophysics, have been provided by [32]. As can be seen in Fig. 7, the theoretical energy dependence of the resulting S factor is slightly steeper than the data, although there is general agreement in magnitude. In the energy range covered by the measurement, the proton width is smaller than the neutron width (except close to the threshold) and thus uncertainties in the description of the proton width (and proton transmission coefficient) will fully impact the resulting S factor. A recent investigation [1] suggested that the strength of the imaginary part of the microscopic potential should be increased by 70%. We find that the energy-dependence of the theoretical S factor is changed in such a way as to show perfect agreement with the new data, as seen in Fig. 7. This independently confirms the conclusions of previous work [1].

G. Astrophysical reaction rates

Regarding the Coulomb suppression effect, a comparison of $1.03 \leq f_{pn} \leq 1.08$ and $2.6 \leq f_{np} \leq 3.9$ shows that the transitions to excited states of ^{85}Sr are more important than those to states in ^{85}Rb in the relevant plasma temperature range of $2 \leq T \leq 4$ GK. The almost negligible stellar enhancement f_{pn} is due to the suppression of the proton transmission coefficients to and from the excited states of ^{85}Rb for small relative proton energies because of the Coulomb barrier. There are only few transitions able to contribute due to the low Q value. As shown by the small f_{pn} , the transition from the ground state of ^{85}Rb dominates the proton channel. Obviously, a Coulomb suppression is not present in the neutron channel. On the contrary, for this reaction f_{np} is even more enhanced due to the spin structure of the available nuclear levels and especially the large spin of $^{85}\text{Sr}^g$. Because of its large spin, it is connected to the (dominating) low spin states in ^{85}Rb through higher partial waves than the excited states, such as the isomeric state, which

have lower spins. Thus, the transitions from the ground state are suppressed by the centrifugal barrier relative to transitions from excited states and the latter will quickly become important, even at low temperature. As a consequence of the enhancement of f_{np} and the suppression of f_{pn} , it is more advantageous to measure the (p,n) direction. Important transitions to states in ^{85}Sr are included in our data and the small impact of transitions from excited states in ^{85}Rb is within the experimental error.

Applying Eq. 2 directly with the experimental cross sections already yields the stellar rate because the SEF is small in the (p,n) direction. The stellar rate of the exothermic (n,p) reaction can then be computed using Eq. (7). By computing the forward rates directly from the backward rates without using fits, the complication with the negative Q value in fitted data is also avoided.

Table X gives the stellar reactivities (as defined by Eq. 4) for $^{85}\text{Rb}(p,n)^{85}\text{Sr}$ as well as for $^{85}\text{Sr}(n,p)^{85}\text{Rb}$. Our data covers an energy range sufficient to compute the rates between 2 and 4 GK. Because of the excellent agreement of theory with experiment (using the newly modified potential of [1]), we supplement the data with the theoretical values to compute the reactivities at lower and higher temperatures, applying the same errors as for the data.

It is to be noted that fits of the rates should be obtained by first fitting the (n,p) rate and then deriving the (p,n) rate fit by modifying the fit coefficients according to detailed balance as given in Eq. (7) (see [11] for details). For convenience, we provide the fit coefficients (including a 10% error) for the (n,p) reactivity in the widely used REACLIB format [11, 17]

$$N_A \mathcal{R}^* = \exp \left(a_0 + \frac{a_1}{T_9} + \frac{a_2}{T_9^{1/3}} + a_3 T_9^{1/3} + a_4 T_9 + a_5 T_9^{5/3} + a_6 \ln T_9 \right), \quad (13)$$

where N_A is Avogadro's number and the plasma temperature $T_9 = T/10^9$, with T in K. Using the usual dimension of $\text{cm}^3 \text{ s}^{-1} \text{ mole}^{-1}$ for $N_A \mathcal{R}^*$ the fitted coefficients evaluate to $a_0 = 33.2271^{+\ln 1.1}_{-\ln 0.9}$, $a_1 = -0.886129$, $a_2 = 40.7296$, $a_3 = -67.9553$, $a_4 = 6.54471$, $a_5 =$

TABLE X: Astrophysical reactivities $N_A \mathcal{R}^*$ of the reactions $^{85}\text{Rb}(p,n)^{85}\text{Sr}$ and $^{85}\text{Sr}(n,p)^{85}\text{Rb}$ computed from experimental data. The values in italics are at temperatures where the experimental data mostly contribute to the rate. The other values are computed by supplementing theoretical cross sections using the modified optical potential.

Temperature [10^9 K]	$^{85}\text{Rb}(p,n)^{85}\text{Sr}$ [$\text{cm}^3\text{s}^{-1}\text{mole}^{-1}$]	$^{85}\text{Sr}(n,p)^{85}\text{Rb}$ [$\text{cm}^3\text{s}^{-1}\text{mole}^{-1}$]
0.10	$(1.72 \pm 0.17) \times 10^{-89}$	$(1.19 \pm 0.2) \times 10^4$
0.15	$(2.21 \pm 0.22) \times 10^{-58}$	$(1.49 \pm 0.15) \times 10^4$
0.20	$(8.33 \pm 0.83) \times 10^{-43}$	$(1.74 \pm 0.17) \times 10^4$
0.30	$(3.36 \pm 0.33) \times 10^{-27}$	$(2.15 \pm 0.22) \times 10^4$
0.40	$(2.26 \pm 0.23) \times 10^{-19}$	$(2.55 \pm 0.26) \times 10^4$
0.50	$(1.18 \pm 0.12) \times 10^{-14}$	$(2.99 \pm 0.30) \times 10^4$
0.60	$(1.74 \pm 0.17) \times 10^{-11}$	$(3.49 \pm 0.35) \times 10^4$
0.70	$(3.31 \pm 0.33) \times 10^{-9}$	$(4.09 \pm 0.41) \times 10^4$
0.80	$(1.77 \pm 0.18) \times 10^{-7}$	$(4.80 \pm 0.48) \times 10^4$
0.90	$(4.04 \pm 0.40) \times 10^{-6}$	$(5.62 \pm 0.56) \times 10^4$
1.00	$(5.07 \pm 0.51) \times 10^{-5}$	$(6.57 \pm 0.66) \times 10^4$
1.50	$(1.28 \pm 0.13) \times 10^{-1}$	$(1.35 \pm 0.14) \times 10^5$
2.00	(8.30 ± 0.83)	$(2.56 \pm 0.26) \times 10^5$
2.50	$(1.21 \pm 0.12) \times 10^2$	$(4.57 \pm 0.46) \times 10^5$
3.00	$(8.22 \pm 0.82) \times 10^2$	$(7.81 \pm 0.78) \times 10^5$
3.50	$(3.56 \pm 0.36) \times 10^3$	$(1.28 \pm 0.13) \times 10^6$
4.00	$(1.15 \pm 0.12) \times 10^4$	$(2.04 \pm 0.20) \times 10^6$
4.50	$(3.03 \pm 0.30) \times 10^4$	$(3.17 \pm 0.32) \times 10^6$
5.00	$(6.89 \pm 0.69) \times 10^4$	$(4.76 \pm 0.48) \times 10^6$
6.00	$(2.60 \pm 0.26) \times 10^5$	$(9.52 \pm 0.95) \times 10^6$
7.00	$(7.14 \pm 0.71) \times 10^5$	$(1.54 \pm 0.15) \times 10^7$
8.00	$(1.50 \pm 0.15) \times 10^6$	$(2.01 \pm 0.20) \times 10^7$
9.00	$(2.50 \pm 0.25) \times 10^6$	$(2.18 \pm 0.22) \times 10^7$
10.00	$(3.44 \pm 0.34) \times 10^6$	$(2.05 \pm 0.21) \times 10^7$

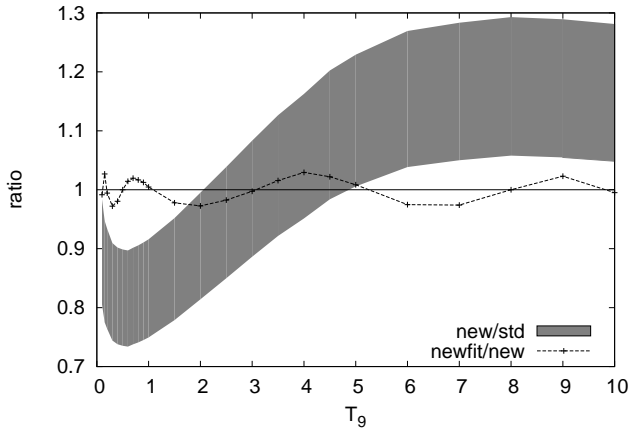


FIG. 8: The newly derived stellar reactivity of $^{85}\text{Sr}(n,p)^{85}\text{Rb}$ is compared to the one given in [33] (area labelled “new/std”). The temperatures T_9 are stellar plasma temperatures in GK. The shaded area accounts for an error of $\pm 10\%$. As seen in Table X, the experimental data contribute significantly in the range $2 \leq T_9 \leq 4$. Also shown is the reactivity from a fit of our new result compared to the actual value (curve labelled “newfit/new”). This shows that the fit accuracy is high.

-0.562194 , $a_6 = 31.1997$. The assumed error is contained in the error given for a_0 . The coefficients for the (p,n) direction are the same, except $a_0^{\text{pn}} = 33.44895^{+\ln 1.1}_{-\ln 0.9}$ and $a_1^{\text{pn}} = -22.3196405$. According to Eqs. (4) and (7), to obtain the final (p,n) rate the value obtained with the seven parameter expression has to be multiplied not only by the number densities of the interacting particles but also by the ratio of the temperature-dependent partition functions of initial and final nucleus

$$N_A \mathcal{R}'_{\text{pn}}(T) = \exp \left(a_0^{\text{pn}} + \frac{a_1^{\text{pn}}}{T_9} + \frac{a_2}{T_9^{1/3}} + a_3 T_9^{1/3} + a_4 T_9 + a_5 T_9^{5/3} + a_6 \ln T_9 \right), \quad (14)$$

$$N_A \mathcal{R}_{\text{pn}}^*(T) = \frac{G_{^{85}\text{Sr}}(T)}{G_{^{85}\text{Rb}}(T)} N_A \mathcal{R}'_{\text{pn}}(T). \quad (15)$$

The required partition functions $G(T)$ are provided in [11] as a function of temperature.

Figure 8 shows a comparison of the new $^{85}\text{Sr}(n,p)^{85}\text{Rb}$ reactivity to the “standard” one of [33]. At temperatures above 3 GK, we see an increase of 10 – 30% compared to the previous values. Below 2 GK, the new reactivity is 20 – 30% lower than previously. The change in the temperature dependence is due to the different proton optical potential used. At very low temperature, the reactivity becomes less sensitive to the proton potential. This explains the ratio becoming almost unity towards zero temperature. Also shown in Fig. 8 is a comparison between the fit of the new reactivity with the parameters above and the reactivity itself. This ratio stays close to unity for all temperatures. The deviations between the reactivity and its fit are very small and negligible compared to the other uncertainties involved.

IV. SUMMARY

We showed that – contrary to common wisdom – a large number of endothermic reactions exhibit smaller stellar enhancement than their exothermic counterparts and are thus preferable for experimental studies. The main cause of suppression of the SEF in an endothermic reaction is the Coulomb suppression of transitions with low relative energy. This Coulomb suppression of the SEF was found to act for reactions with $Q < 0$ but low $|Q|$ and charged projectiles. Allowing only nucleons, α particles, and photons as projectiles or ejectiles, and restricting the results to experimentally useful values of the SEFs, this effect still appears in 1200 reactions, including α captures relevant in the p process [5, 6] and proton captures relevant in the rp process [15] and the νp process [16]. A large number of cases was also found for (p,n) reactions which allow to determine astrophysical reaction rates relevant to the γ process [6].

As an example, we measured the astrophysically important reaction $^{85}\text{Rb}(p,n)^{85}\text{Sr}$ close above the threshold in the energy range relevant for the γ process. It

was shown that in this case it is possible to derive astrophysical reaction rates for the (n,p) as well as the (p,n) direction directly from the (p,n) data despite of the negative reaction Q value. Additionally, our measurement confirms a previously derived modification of the global proton optical potential used in theoretical predictions.

Acknowledgments

This work was supported by the European Research Council grant agreement no. 203175, the Economic Com-

petitiveness Operative Programme GVOP-3.2.1.-2004-04-0402/3.0., OTKA (K68801, T49245), and the Swiss NSF (grant 2000-105328). Gy. Gy. acknowledges support from the Bolyai grant.

-
- [1] G. G. Kiss, Gy. Gyürky, Z. Elekes, Zs. Fülöp, E. Somorjai, T. Rauscher, and M. Wiescher, *Phys. Rev. C* **76**, 055807 (2007).
 - [2] S. E. Woosley and W. M. Howard, *Astrophys. J. Suppl.* **36**, 285 (1978).
 - [3] M. Arnould and S. Goriely, *Phys. Rep.* **384**, 1 (2003).
 - [4] T. Rauscher, A. Heger, R. D. Hoffman, and S. E. Woosley, *Astrophys. J.* **576**, 323 (2002).
 - [5] T. Rauscher, *Phys. Rev. C* **73**, 015804 (2006).
 - [6] W. Rapp, J. Görres, M. Wiescher, H. Schatz, and F. Käppeler, *Astrophys. J.* **653**, 474 (2006).
 - [7] G. G. Kiss, T. Rauscher, Gy. Gyürky, A. Simon, Zs. Fülöp, E. Somorjai, *Phys. Rev. Lett.* **101**, 191101 (2008).
 - [8] C. Iliadis, *Nuclear Physics of Stars* (Wiley, Weinheim 2007).
 - [9] W. A. Fowler, *Quart. J. Roy. Astron. Soc.* **15**, 82 (1974).
 - [10] J. A. Holmes, S. E. Woosley, W. A. Fowler, and B. A. Zimmerman, *At. Data Nucl. Data Tables* **18**, 305 (1976).
 - [11] T. Rauscher and F.-K. Thielemann, *At. Data Nucl. Data Tables* **75**, 1 (2000).
 - [12] H. Utsunomiya, P. Mohr, A. Zilges, and M. Rayet, *Nucl. Phys. A* **777**, 459 (2006).
 - [13] P. Mohr, Zs. Fülöp, and H. Utsunomiya, *Eur. Phys. J. A* **32**, 357 (2007).
 - [14] T. Rauscher and F.-K. Thielemann, in *Stellar Evolution, Stellar Explosions, and Galactic Chemical Evolution*, ed. A. Mezzacappa (IOP, Bristol 1998), p. 519.
 - [15] H. Schatz *et al.*, *Phys. Rep.* **294**, 167 (1998).
 - [16] C. Fröhlich, *et al.*, *Phys. Rev. Lett.* **96**, 142502 (2006).
 - [17] J. J. Cowan, F.-K. Thielemann, and J. W. Truran, *Phys. Rep.* **208**, 267 (1991).
 - [18] M. Arnould, S. Goriely, and K. Takahashi, *Phys. Rep.* **450**, 97 (2007).
 - [19] T. Rauscher, F.-K. Thielemann, and K.-L. Kratz, *Phys. Rev. C* **56**, 1613 (1997).
 - [20] C. Freiburghaus, F. Rembges, T. Rauscher, E. Kolbe, F.-K. Thielemann, K.-L. Kratz, B. Pfeiffer, and J. J. Cowan, *Astrophys. J.* **516**, 381 (1999).
 - [21] K. Farouqi, K.-L. Kratz, B. Pfeiffer, T. Rauscher, F.-K. Thielemann, and J. W. Truran, submitted to *Astrophys. J.* (2009).
 - [22] I. Dillmann, T. Rauscher, M. Heil, F. Käppeler, W. Rapp, and F.-K. Thielemann, *J. Phys. G* **35**, 014029 (2008).
 - [23] <http://nucleardata.nuclear.lu.se/nucleardata/toi/>
 - [24] S. Kastleiner, S. M. Qaim, F. M. Nortier, G. Blessing, T. N. van der Walt, and H. H. Coenen, *Appl. Radiat. Isot.* **56**, 685 (2002).
 - [25] I. Rajta, I. Borbély-Kiss, Gy. Mórík, L. Bartha, E. Koltay and Á. Z. Kiss, *Nucl. Instr. Meth.* **B118**, 437 (1996).
 - [26] A. Simon, T. Csákó, C. Jeynes, and T. Sörényi, *Nucl. Instr. Meth.* **B249**, 454 (2006).
 - [27] C. Yalcin, R. T. Güray, N. Özkan, S. Kutlu, Gy. Gyürky, J. Farkas, G. G. Kiss, Zs. Fülöp, A. Simon, E. Somorjai, and T. Rauscher, *Phys. Rev. C* **79**, 065801 (2009).
 - [28] E. Kótai, *Nucl. Instr. Meth.* **B85**, 588 (1994).
 - [29] H. Siever, *Nucl. Data Sheets* **62**, 271 (1991).
 - [30] J. F. Ziegler and J. P. Biersack, code SRIM Version 2003.20
 - [31] J. P. Jeukenne, A. Lejeune, and C. Mahaux, *Phys. Rev. C* **16**, 80 (1977).
 - [32] A. Lejeune, *Phys. Rev. C* **21**, 1107, (1980).
 - [33] T. Rauscher and F.-K. Thielemann, *At. Data Nucl. Data Tables* **79**, 47 (2001).